A Novel Scheme for Extracting Sea Surface Wind Information From Rain-Contaminated X-Band Marine Radar Images

Xinwei Chen, *Student Member, IEEE*, Weimin Huang, *Senior Member, IEEE*, and Merrick C. Haller, *Senior Member, IEEE*

***Abstract*—The presence of rain degrades the performance of sea surface parameter estimation using X-band marine radar. In this article, a novel scheme is proposed to improve wind measurement accuracy from rain-contaminated X-band marine radar data. After extracting texture features from each image pixel, the rain-contaminated regions with blurry wave signatures are first identified using a self-organizing map (SOM)-based clustering model. Then, a convolutional neural network used for image haze removal, i.e., DehazeNet is introduced and incorporated into the proposed scheme for correcting the influence of rain on radar images. In order to obtain wind direction information, curve fitting is conducted on the average azimuthal intensities of rain-corrected radar images. On the other hand, wind speed is estimated from rain-corrected images by training a support vector regression-based model. Experiments conducted using datasets from both shipborne and onshore marine radar show that compared to results obtained from images without rain correction, the proposed method achieves relatively high estimation accuracy by reducing measurement errors significantly.**

***Index Terms*—Image dehazing, rain, wind, X-band marine radar.**

I. Introduction

THE real-time monitoring of sea surface wind information enhances the safety, performance, and efficiency of various weather-sensitive on- and off-shore activities, such as port operations, cargo shipping, and marine resource development (e.g., offshore drilling and windfarming). While conventional *in situ* sensors such as anemometers are usually used for wind measurements, they are susceptible to several factors, such as atmospheric turbulence and the flow distortion caused by superstructure or the movement of the anemometer platform, resulting in inaccurate estimation [1]. Thanks to the development of faster hardware with more memory in the past two decades, X-band marine radar has become a popular ocean remote sensor for sea surface wind, wave, and current parameter measurements due to its high temporal and spatial resolution. In addition, as practically most ships are already equipped with X-band radars for navigational purposes, these wind data can be obtained at a small extra cost [2].

Previous studies [3] and [4] have demonstrated that for X-band radar operating at grazing incidence with horizontal-transmit-horizontal-receive (HH) polarization, its radar backscatter from the ocean surface only exhibits one peak, which lies in the upwind direction. Thus, wind direction can be derived from the dependence of backscatter intensity on the relative azimuth between antenna look direction and wind direction. As for wind speed, it can be retrieved by establishing an empirical model relating wind speed to backscatter intensity information extracted from the radar data. Based on this principle, multiple wind parameter estimation methods have been proposed. Some of them [5]–[8] require temporal-integrated radar images for wind retrieval, while others can estimate wind parameters from individual images directly [2], [9]. Although satisfactory measurement results were demonstrated with data from shipborne and onshore marine radars, it has been found that under the presence of rain, the performance of the methods mentioned above might be negatively affected. That is because X-band radio wave is scattered and attenuated by rainfall in the atmosphere, and the sea surface roughness is altered by rain drops as well [10]. Consequently, the ocean waves imaged by the radar are blurred, causing inaccurate measurements. Thus, in these studies, radar data contaminated by precipitation were first identified and then excluded from wind retrieval. In recent years, a series of works [11]–[16] managed to recycle the rain-contaminated data and applied novel or modified algorithms for wind retrieval, which improved the estimation accuracy under rain conditions. Nevertheless, those methods still have certain limitations. For example, no strategy has been undertaken to conduct pixel-based rain detection or to correct the influence of rain on radar images. In addition, as those methods were only validated using the same shipborne marine radar image dataset, whether they can still perform generally well using other datasets remains unknown. Thus, a novel scheme for determining wind parameters from

Manuscript received November 30, 2020; revised January 12, 2021 and April 27, 2021; accepted May 7, 2021. Date of publication May 11, 2021; date of current version May 31, 2021. The work of Weimin Huang was supported by the Natural Sciences and Engineering Research Council of Canada (NSERC) Discovery Grants under Grant NSERC RGPIN-2017-04508 and Grant RGPAS-2017-507962. This work was supported by the Mitacs through the Mitacs Accelerate Program (IT21291 and IT20702). *(Corresponding authors: Xinwei Chen; Weimin Huang.)*

Xinwei Chen and Weimin Huang are with the Faculty of Engineering and Applied Science, Memorial University of Newfoundland, St. John's, NL A1B 3X5, Canada (e-mail: xinweic@mun.ca; weimin@mun.ca).

Merrick C. Haller is with the School of Civil & Construction Engineering, Oregon State University, Corvallis, OR 97331 USA (e-mail: merrick.haller@oregonstate.edu).

Digital Object Identifier 10.1109/JSTARS.2021.3078902

rain-contaminated data with pixel-based rain correction techniques incorporated is worth pursuing.

Following the common practice in radar data processing, the proposed scheme should consist of three major procedures: Detecting the presence of rain, mitigating the influence of rain, and estimating wind parameters from rain-corrected radar images. It was found in [14] that the influence of rain on different portions of the radar image may differ. Specifically, in a rain-contaminated radar image, some regions may still remain unaffected by rain. Hence, rain-contaminated regions need to be identified first before introducing rain mitigation techniques. In [17], Chen and Huang proposed a self-organizing map (SOM)-based model to classify between rain-free and rain-contaminated regions in a single radar image with relatively high accuracy, which can be incorporated into the first step of the proposed scheme directly. While the method for detecting rain-contaminated regions can be applied directly, no mature rain correction techniques are available for our application. That is because little is known about the dominant backscatter mechanism for X-band marine radars operating at grazing incidence in presence of rain [2], which hinders the studies concerning correcting the influence of rain on radar images. Although in recent years, many other image correction problems have been successfully tackled using the latest machine learning techniques, a lack of corresponding "ground truth" rain-free images for model training makes it impossible to build the rain correction model from scratch.

In contrast to rain mitigation, analyzing and mitigating the influence of haze on terrestrial images is a hot research topic with numerous papers being published in the past decade. In this study, many similarities have been observed between the influence of rain on marine radar images and the influence of haze on terrestrial photography, which enables us to apply image dehazing techniques on rain correction with certain modifications. In particular, a type of convolutional neural network (CNN)-based image dehazing model, named as DehazeNet, proposed by Cai *et al.* [18] is not only superior in performance but also efficient and easy to use, which can be considered as the basis of the rain correction model. As for the third step, i.e., wind measurements, in the past few years, machine learning-based regression algorithms have been introduced to estimate wind speed and significant wave height from marine radar data [16], [19], [20] with higher accuracy and robustness in comparison with traditional methods, which can be incorporated into the proposed scheme.

In this article, a novel scheme for wind parameter estimation using rain-contaminated X-band marine radar data based on the techniques mentioned above is presented. This is the first work to apply the pixel-based rain identification model for sea surface parameter estimation from X-band marine radar data under rain conditions. Also, instead of just identifying rain-contaminated pixels like [17] without any further processing, the DehazeNet is introduced and incorporated into the proposed scheme for correcting the influence of rain on those pixels. While the cosine-squared function proposed in [2] is applied for wind direction estimation, modifications have been made on the curve fitting procedure in order to improve the robustness of the estimation results under rain conditions. As for the support vector regression (SVR)-based wind speed estimation method, although the settings of the SVR algorithm (e.g., kernel function and training solver) are based on [16], the feature vectors input into the model are extracted from the texture feature maps of the rain-corrected radar image and those feature maps contain the information about the spatial variation of the radar image. In contrast, the feature vector of the SVR model in [16] only consists of histogram-based features extracted from the original radar image, which does not preserve the spatial information of the radar image and might not perform well in the presence of rain. Thus, extracting texture map-based features from rain-contaminated images significantly improves the estimation accuracy of the SVR model under rain conditions. The remainder of the article is organized as follows. A detailed illustration of all the models and algorithms employed in each step of the proposed scheme is given in Section II. Section III presents an overview of the radar datasets used in this study followed by experimental results obtained from real radar data. A summary with discussions appears in Section IV.

II. Proposed Scheme for Wind Estimation

A. Framework of the Proposed Scheme

Fig. 1 shows the framework of the proposed method for rain mitigation and wind estimation. Texture features extracted from each pixel of the radar image are input into the SOM-based clustering model proposed in [17], which generates rain-contaminated region identification results. Images contaminated by rain are then subjected to the rain correction procedure based on the DehazeNet proposed in [18]. After obtaining rain-corrected radar images, curve fitting techniques are used to measure wind direction, while a modified SVR-based model is trained for wind speed estimation.

B. SOM-Based Rain-Contaminated Region Identification

Fig. 2 illustrates the SOM-based identification model. Since it has been found in [14] that the texture of rain-contaminated echoes is different from that of less-contaminated or rain-free echoes, four types of texture features are first extracted from each pixel and combined as a 55D feature vector. Each type of texture feature is briefly introduced below.

1) *Gabor Features*: The Gabor filter bank is a set of Gaussian-shaped band-pass filters, which has been widely used for texture analysis due to its similarity with human visual system in frequency and orientation representations [21]. The Gabor filter bank constructed in [17] with 4 orientations and 6 wavelengths is used to filter each radar image and produce 24 Gabor feature maps.
2) *Wavelet Features*: In previous studies, wavelet transform has been applied for wave [22] and bathymetry [23] inversion using X-band marine radar data. Here, 1D discrete wavelet transform (DWT) is applied to each radar image, which generates four feature maps consisting of four channels (i.e., low-low, low-high, high-low, high-high). After upsampling the four channels to the same size as the radar image, the standard deviation filtering is then performed on each output channel image, producing the

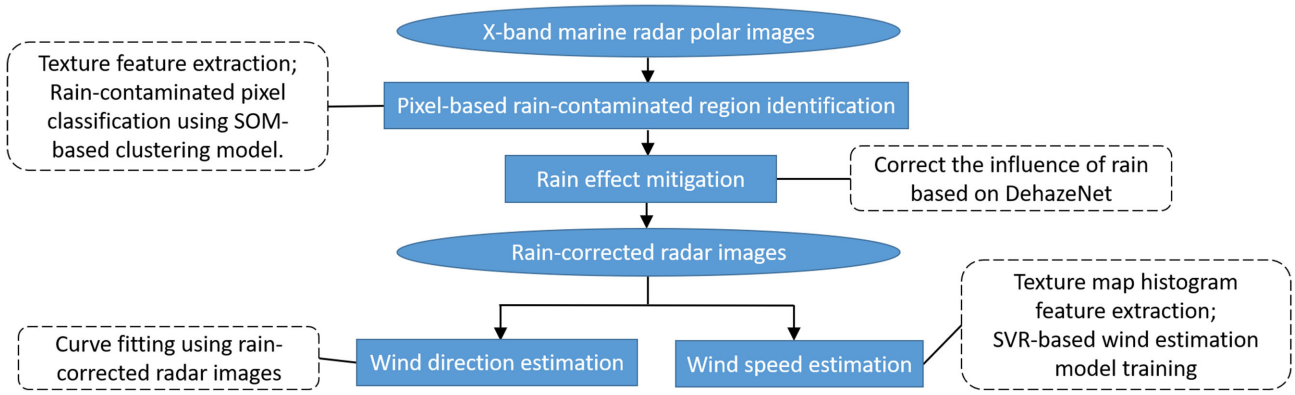

Fig. 1. Flowchart of the proposed scheme for sea surface wind measurements from rain-contaminated marine radar images.

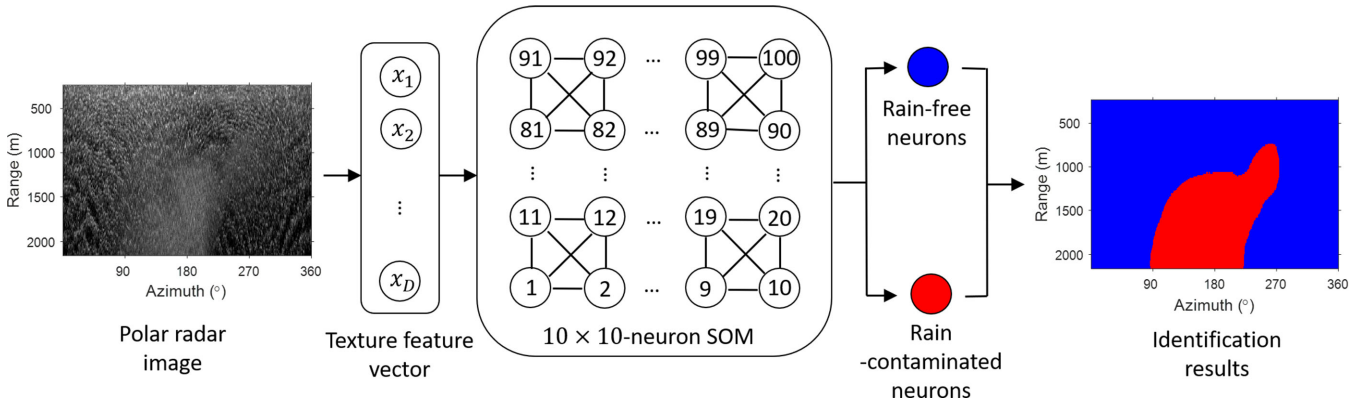

Fig. 2. SOM-based rain-contaminated region identification. The radar data presented on the left is described in Section III-A.

corresponding local standard deviation image. Hence, an 8D feature vector can be derived for each pixel.

3) *Discrete Cosine Transform (DCT)-Based Features*: A set of filters consisting of nine 3×3 orthogonal DCT masks proposed in [24] is used to generate the DCT features. Since the mask with low-pass property is excluded from feature combination, 8 DCT feature maps can be generated.

4) *Local Histogram Features*: As it has been observed in [16] that rain alters the pixel distribution, i.e., histogram, of the radar image [a comparison between the normalized histogram of a rain-free and rain-contaminated image is shown in Fig. 3(d)], for each pixel its local histogram feature vector is obtained from the histogram of a moving window with respect to the center pixel. Since the moving window is supposed to cover a range of around 200 m and an azimuth of around 10°, its size is determined by the image resolution. It should also be noted that pixel intensities between 0 and 150 are used to generate the normalized histogram with a bin size of 10, while pixel intensities larger than 150 are discarded from feature extraction.

As one of the most popular unsupervised neural networks, the SOM looks for patterns previously undetected in a dataset with no preexisting labels. In other words, it is able to classify data automatically without human supervision. It is well known that for supervised training techniques such as backpropagation, the training data consist of vector pairs, i.e., an input vector and a target vector. With this approach an input vector is presented to the network (typically a multilayer feedforward network) and the output is compared with the target vector. If they are different, the weights of the network are altered slightly to reduce the error in the output. This is repeated many times with many sets of vector pairs until the network obtains the desired output. In contrast, training an SOM requires no target vector. The training of SOM begins with initializing each weight vector that represents a certain neuron. From there an input vector (i.e., the texture feature vector in this study) is selected randomly and the map of weight vectors is searched to find which weight (a certain neuron) best represents that input vector. Each weight vector has neighboring weights that are close to it. The weight that is chosen (denoted as the winning neuron) is rewarded by being able to become more like that randomly selected sample vector. The neighbors of the winning neuron are also rewarded by being able to become more like the chosen input vector. The closer a neuron is to the winning neuron, the more its weight gets altered. In contrast, the farther the neighbor is away from the winning neuron, the less it learns. In addition, the number of neighbors and how much each weight is altered decrease over time. This whole process is repeated a large number of times until the preset iteration time is reached. Compared to the input texture feature vector with relatively high dimension, the neurons in the proposed SOM

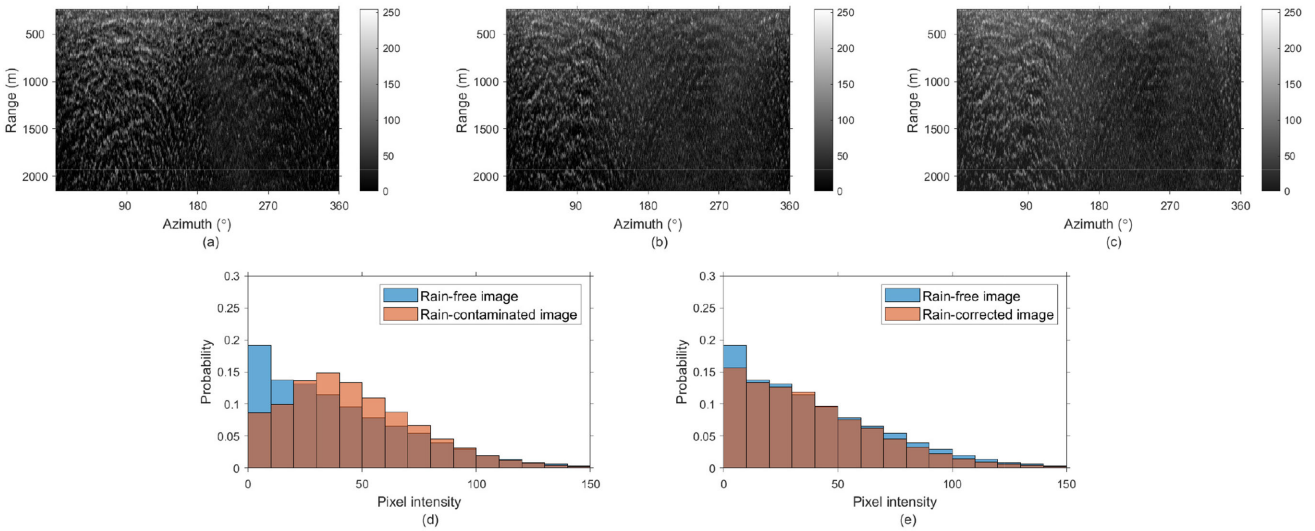

Fig. 3. (a) Example of a rain-free, (b) Rain-contaminated, and (c) its corresponding rain-corrected radar image obtained in the same region under similar wind speeds. Comparisons of their normalized histograms are presented in (d) and (e).

are arranged in a single, 2D grid in the shape of rectangles, which provides a way of representing multidimensional data in spaces of much lower dimension. Nevertheless, the topological relationships within the training set are still maintained, which means feature vectors that are close in the feature space tend to be clustered into the same or topological neighboring neurons. In this work the texture feature vector extracted from each pixel, denoted as $X = \{x_i, i = 1, \ldots, D\}, D = 55$, is input into the 10 $\times$ 10-neuron SOM constructed and trained in [17]. Each neuron is represented by a weight vector $v_j = \{v_{ji} : j = 1, \ldots, N; i = 1, \ldots, D\}$, where N is the total number of neurons (100 here). In order to classify each feature vector into a certain class, the Euclidean distance between X and each neuron is calculated and X is classified into the neuron with the smallest distance, which can be expressed as

$$j = \arg\min_{j} \sum_{i=1}^{D} (x_i - v_{ji})^2. \tag{1}$$

As in [17], neurons were already clustered into three types (rain-free, rain-contaminated, and low-backscatter) using a hierarchical clustering tree, pixel-based identification results can be obtained directly. It should be noted that in this study, neurons classified as low-backscatter type are also considered as rain-free since low-backscatter radar images are caused by low sea states instead of rain. Hence, given a polar radar image I, its corresponding identification result P can be represented as a binary image

$$P(\theta, r) = \begin{cases} 0, & \text{if } I(\theta, r) \text{ is clustered into a rain-free neuron} \\ 1, & \text{if } I(\theta, r) \text{ is clustered into a rain-contaminated neuron} \end{cases} \tag{2}$$

where θ and r represent azimuth direction coordinate and range coordinate, respectively.

C. DehazeNet-Based Rain-Contaminated Region Correction

In recent years, significant progresses have been made on terrestrial image haze removal thanks to the important assumptions and priors about the influence of haze on images proposed in previous studies [25]–[27]. While there are many differences in the physical process between rain affecting sea surface and radio waves and haze scattering atmospheric light, it has been observed in this study that rain-contaminated radar images also conform to those assumptions, which makes it reasonable to apply image dehazing algorithms on rain correction. Here, the similarities between the influence of rain on marine radar images and the influence of haze on terrestrial photography based on those assumptions/priors are first illustrated below.

(1) *Reduction of "Dark" Pixel Proportion*: Previous statistical observation has found that in most of the haze-free patches of terrestrial photography, their minimum intensities in one or more certain channels should have very low values or even close to zero. That assumption is referred to as dark channel prior in [26]. In contrast, patches affected by haze generally look brighter than haze-free ones due to the scattering introduced by haze. As a result, it is common that none of the channels has pixels with very low intensities. Likewise, for rain-free marine radar image regions, the "dark" pixels located in areas shadowed by surface wave crests generally have very low backscatter intensities. Consequently, as presented by the blue bins in Fig. 3(d), the first bin of the normalized histogram obtained from a rain-free image [i.e., Fig. 3(a)] should have a relatively significant portion. While for the rain-contaminated image shown in Fig. 3(b), it is uniformly bright [28] with a relatively low value in the first bin of its normalized histogram, as shown by the orange bins in Fig. 3(c).

(2) *Reduction of Local Contrast*: It has been widely acknowledged that terrestrial photography with enhanced

visibility (or clear-day images) has higher contrast than images obtained under bad weather such as the presence of haze. Based on the definition of RGB image contrast proposed in [25], the contrast $C(I)$ of a grayscale radar image $I(\theta, r)$ can be quantitatively defined as

$$C(I) = \sum_{\theta,r} |\nabla I(\theta, r)| \tag{3}$$

where ∇ is the differential operator over azimuth and range coordinate. By observing the radar dataset, the contrast of a radar image contaminated by rain is significantly lower than a rain-free image obtained under similar wind speeds.

(3) *Reduction of Local Saturation*: Based on the definition of saturation in an RGB image patch proposed in [27], the saturation of a radar image patch $S(I)$ can be expressed as

$$S(I) = \frac{\max(I(\theta, r)) - \min(I(\theta, r))}{\max(I(\theta, r))}. \tag{4}$$

As the decline of saturation under the influence of haze has been widely observed, it is also found here that the saturation of a rain-contaminated radar image region is generally lower than a rain-free region obtained under similar wind speeds.

Designed and trained by Cai *et al.* [18], DehazeNet is a CNN-based end-to-end system for single image haze removal. The reasons of adopting DehazeNet instead of other AI models for rain correction are explained as follows. First, as an end-to-end neural network, DehazeNet is able to take the whole original radar image as an input and generate its corresponding transmission map directly without additional processing steps, which is both efficient and easy to use. Second, as illustrated in Section II-C, it has been observed that the effect of haze on terrestrial images and the influence of rain on marine radar images are similar on several assumptions (e.g., reduction of "dark" pixel proportion, reduction of local contrast, and reduction of local saturation). Compared to other AI models or previous proposed image dehazing models that are based on a single assumption (e.g., [26] and [25]), DehazeNet takes all of those assumptions into consideration in its feature extraction step, which improves the performance of the model in haze removal and rain correction. In addition, compared to other CNNs with classical architecture, several modifications are made in the components and structure of DehazeNet, which further improves the robustness and efficiency of the model. For example, instead of using standard nonlinear activation functions in deep networks such as rectified linear unit (ReLU), a novel nonlinear activation function, i.e., bilateral rectified linear unit (BReLU), is proposed and applied in DehazeNet. As ReLU is mainly used for the problems of classification, BReLU is specifically designed for regression problems, which can reduce search space and improve convergence during the training process. Fig. 4 shows the framework of the proposed rain correction method based on DehazeNet with each step elaborated below.

1) Haze-Relevant Feature Extraction: As the first step of operation conducted by the DehazeNet, a variety of features based on those haze-related assumptions/priors are extracted through

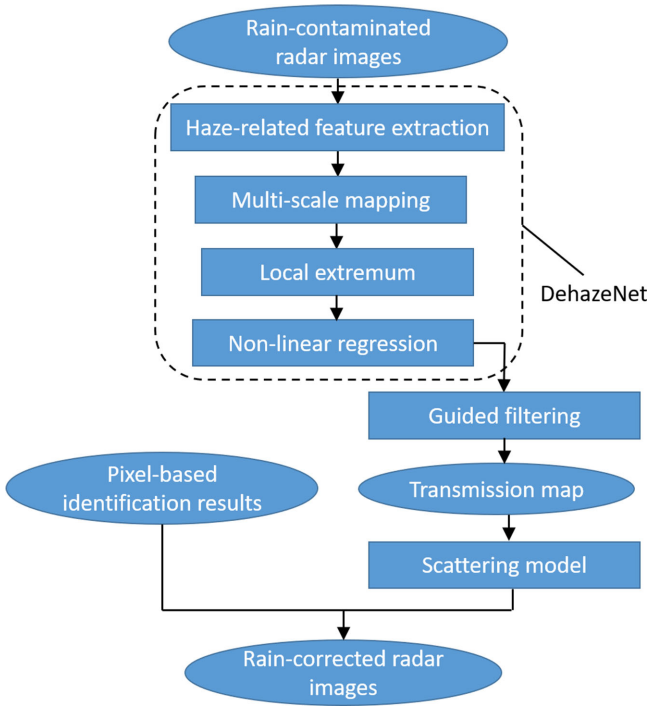

Fig. 4. Flowchart of the proposed rain correction method based on DehazeNet.

convolution. While DehazeNet differs from other typical CNNs in structure, convolution is still one of the main building blocks. The term convolution refers to the mathematical combination of two functions to produce a third function which merges two sets of information. In the case of a CNN, each convolution operation is performed on the input data with the use of a filter (or kernel) to produce a feature map, which is executed by sliding the filter over the input. At every location, a matrix multiplication is performed and the result in the feature map is the sum of the element-by-element product. Since the network is originally used to process RGB images, each rain-contaminated radar image is first converted into RGB format by replication before inputting the image into the network. Sixteen $5 \times 5 \times 3$ filters, denoted as W_1^i $(i = 1, \ldots, 16)$, are first convolved with the radar image, which generates 16 haze-related feature maps (denoted as f_1) expressed as

$$f_1^i = W_1^i * I + B_1^i \tag{5}$$

where $*$ and B_1^i represent the convolution operation and the bias term for each filter, respectively. Then, an unusual activation function called maxout unit is introduced to reduce the dimension of the feature maps, which generates a new feature map by taking a pixel-wise maximization operation for every 4 consecutive feature maps, which can be expressed as

$$F_1^k(\theta, r) = \max_{i \in \{0,1,2,3\}, k \in \{1,2,3,4\}} f_1^{k \times 4 - i}(\theta, r). \tag{6}$$

Therefore, a total of four feature maps can be generated after the feature extraction steps.

2) Multiscale Feature Generation: In this step, filters with different spatial scales (i.e., 3×3, 5×5, and 7×7) are used to filter F_1 in order to generate multiscale features, which have been proven effective for haze removal [29]. Since 16 filters

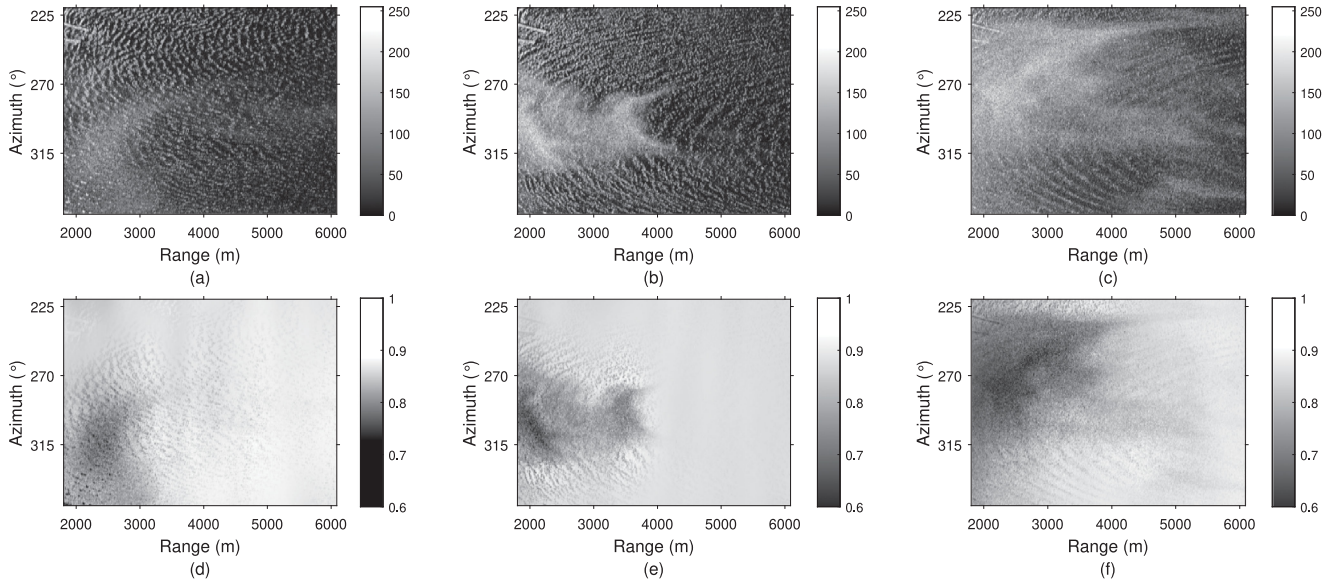

Fig. 5. (a)–(c) Examples of X-band marine radar images with rain-contaminated regions. (d)–(f) Transmission map obtained from (a)–(c) using the DehazeNet. The radar data presented here is described in Section III-A.

are assigned for each selected filter size, a total of 48 feature maps, denoted as F_2^i ($i = 1, \ldots, 48$), can be generated using the convolution operation in (5).

3) Local Extremum: The max-pooling layer calculates and preserves the maximum value for each patch of the feature map in order to reduce the number of parameters and computation in the network. In this way, the training time can be shortened and overfitting can be better avoided. However, since the size of the final output image in DehazeNet is supposed to be the same as the input image's, the traditional max-pooling operation is replaced by another type of operation named as local extremum in [18], in which the original image size is retained while the local maximum values can still be extracted. Specifically, for each pixel in the feature map F_2^i, its local extremum equals the maximum value in a 7×7 window centered at this pixel. Thus, the output feature maps F_3^i ($i = 1, \ldots, 48$) obtained from local extremum operation can be expressed as

$$F_3^i(\theta_0, r_0) = \max_{\theta, r \in \Omega(\theta_0, r_0)} F_2^i(\theta, r) \tag{7}$$

where $\Omega(\theta_0, r_0)$ is the 7×7 neighborhood centered at the pixel located at (θ_0, r_0). In this way, the size of the output image remains the same as the input image.

4) Nonlinear Regression: Activation functions perform a nonlinear transformation on the input received, which keep values within a manageable range. Since values in the input layers are generally centered at zero and have already been appropriately scaled, they do not require transformation in the first place. However, the range of these values becomes much larger after they are multiplied by weights and summed together during the convolution operation. Thus, the activation functions should be introduced after convolution, which force values back within an acceptable range and make them meaningful. For classic CNNs, an activation function is normally applied to the filtering outputs for nonlinear regression and approximation. In the DehazeNet, a novel activation function modified from the rectified linear unit (ReLU) called bilateral ReLU is used to regress and generate the network output F_4, which can be expressed as

$$F_4 = \min(t_{\max}, \max(t_{\min}, F_3 * W_4 + B_4)) \tag{8}$$

where W_4 and B_4 represent a $6 \times 6 \times 48$ filter and its corresponding bias, respectively. $t_{\min}$ and $t_{\max}$ are the marginal values limiting the minimum and maximum of the regression output, which equal 0 and 1, respectively.

5) Rain-Corrected Radar Image Generation: As shown in Fig. 4, the output image obtained from the DehazeNet, i.e., F_4, is input into the guided filters proposed in [30] for edge-preserving smoothing. The filtering output, denoted as $t(\theta, r)$, is called the transmission map, which is used to describe the light portion that is not scattered and reaches the camera in terrestrial photography. In this study, the transmission map generated from rain-contaminated radar image can be used to reflect the degree of rain influence. That is because it has been observed that regions contaminated by heavy rain generally have much lower corresponding pixel intensities in the transmission map than those less affected or unaffected by rain (see a few examples presented in Fig. 5). Hence, the formulation of the atmospheric scattering model obtained from previous studies [25], [31], [32] is introduced to suppress the rain echoes in the original radar image. Its output of each pixel, denoted as $J(\theta_0, r_0)$, can be calculated as

$$J(\theta_0, r_0) = \frac{I(\theta_0, r_0) - \max(I)}{t(\theta_0, r_0)} + \max(I) \tag{9}$$

where the intensity range of I has been scaled to [0,1]. Finally, $J(\theta, r)$ is combined with the rain-contaminated region identification results ($P(\theta, r)$) to generate the rain-corrected radar image with smooth transition between rain-free and

rain-contaminated regions. Specifically, for each radar image consisting of both rain-free and rain-contaminated regions, if c_1 and c_2 denote the centroids of rain-free and rain-contaminated regions, respectively, the Euclidean distances between each pixel $I(\theta_0, r_0)$ and c_1, c_2 are obtained and expressed as $d_1(\theta_0, r_0), d_2(\theta_0, r_0)$. Each pixel of the rain-corrected image $L(\theta_0, r_0)$ is then calculated as

$$L(\theta_0, r_0) = \begin{cases} I(\theta_0, r_0) + \dfrac{d_1(\theta_0, r_0)[J(\theta_0, r_0) - I(\theta_0, r_0)]}{5[d_1(\theta_0, r_0) + d_2(\theta_0, r_0)]} \\ \qquad \text{if } P(\theta_0, r_0) = 0 \\ J(\theta_0, r_0) + \dfrac{d_2(\theta_0, r_0)[I(\theta_0, r_0) - J(\theta_0, r_0)]}{d_1(\theta_0, r_0) + d_2(\theta_0, r_0)} \\ \qquad \text{if } P(\theta_0, r_0) = 1. \end{cases} \tag{10}$$

It should be noted that (10) is only applicable for images with both rain-free and rain-contaminated regions. For a rain-contaminated image without any rain-free regions, its corresponding rain-corrected result equals to $J(\theta_0, r_0)$ directly. Also, it should be noted that the intensity range of I has been scaled to [0, 1].

In [18], the training of DehazeNet has been illustrated in detail and will be introduced briefly here. First, in order to obtain sufficient amount of training data, 10 000 haze-free patches (a patch refers to a subsection of a whole image) are sampled randomly from terrestrial images collected from the Internet. Then, 10 random transmission maps (with values uniformly distributed from 0 to 1) are generated from each patch, which can therefore generate 10 corresponding hazy patches. Hence, a total of 100 000 artificial hazy patches are generated and used to train the network. A Gaussian distribution function (with mean value $\mu = 0$ and standard deviation $\sigma = 0.001$) is introduced to give random values to the filters in each layer of the network, and the initial values of all bias terms are set to be 0. The initial learning rate is set to be 0.005 and will decrease by half for every 100 000 iterations. In each iteration, a total of 128 patches are utilized for training. Based on the parameter settings mentioned above, the DehazeNet can be trained after a total of 500 000 iterations. It should be noted that since the learnable parameters (i.e., filters and biases) of the network are inherited from the training results obtained in [18], the network can be incorporated into the proposed scheme directly without further training.

D. Wind Parameter Estimation Algorithms

After obtaining the rain-corrected radar image, for each azimuthal direction θ, its average pixel intensity (denoted as σ_θ) is calculated and curve fitted using the cosine-squared function proposed by Lund *et al.* [2], which can be expressed as

$$\sigma_\theta = a_0 + a_1 \cos^2(0.5(\theta - a_2)) \tag{11}$$

where a_0, a_1, and a_2 are parameters determined through least-squares fitting. The estimated wind direction corresponds to the azimuth located at the peak of the fitted function. It should be noted that for one certain rain-corrected radar image, the curve fitting is conducted for multiple times (20 in this study), which generates 20 different combinations of coefficients [i.e., a_0, a_1, and a_2 in (11)] for the fitted function. The combination of coefficients with the highest R-squared (coefficient of determination) value, which reflects how close the data are to the fitted regression line, is selected for producing the final fitted curve. The reason to do so is because during each curve fitting, the value for each coefficient is initialized uniformly but randomly from the interval (0,1). As a result, multiple fits using the same data and function might lead to different fitted coefficients. Thus, in order to generate the best fitted curve for each image, it is necessary to repeat the curve fitting for multiple times.

As for wind speed estimation, the SVR-based wind speed estimation model proposed in [16] is modified and trained using the rain-corrected radar images. Specifically, in the feature extraction step, instead of extracting the normalized histogram bin values of the original radar image, several of the texture feature maps (presented in Table I) introduced in the first step of the proposed scheme (i.e., Section II-B) are generated from the rain-corrected radar image and incorporated into the feature vector, which further improves the accuracy and robustness of the model. The first two feature maps generated by two Gabor filters with the same orientation (90°) and two different wavelengths manifest the clarity of the stripe-like wave patterns in the radar image. Although under rain conditions, the sea surface roughness might be altered and wave patterns in the radar image might be blurred, it has been observed that the wave patterns in rain-contaminated images obtained under high wind speeds tend to be less affected or even unaffected in some image regions. An example of a rain-contaminated radar image obtained under high wind speed is presented in Fig. 6(a). It can be observed that regions with clear wave signatures have relatively high intensities in the corresponding pixels of those two Gabor feature maps, as shown in Fig. 6(b) and (c). While for the rain-contaminated radar image obtained under low wind speed presented in Fig. 7(a), the wave patterns are blurred significantly in almost all areas. In consequence, the pixel intensities in its corresponding feature maps, i.e., Fig. 7(b) and (c) are generally much lower than that of Fig. 6(a)'s. As for the third feature map, i.e., the local standard deviation image of the radar image's low-low channel generated by DWT, it is used to reflect of the influence of wind speed and rain on sea surface roughness. It is well known that an increasing wind speed leads to the increase in sea surface roughness [33] as well as average radar backscatter intensity [2]. On the other hand, the change of sea surface roughness due to the presence of rain results in the decrease of pixel intensity variation in rain-contaminated images/regions [34]. For instance, it can be observed from Fig. 6(d), that regions that are less affected by rain with high sea surface roughness and simultaneous wind speed have relatively high intensities. In contrast, the pixel intensities of most pixels in Fig. 7(d) are very low compared to Fig. 6(d) because the sea surface roughness is altered significant by rain with wave patterns barely observed in almost all areas in Fig. 7(a), which also causes fairly uniform pixel intensities in the radar image. Bin values are extracted from the histograms of the texture feature maps presented in Table I. Thus, the feature vector extracted from each image consists of 70 elements.

For a certain rain-corrected radar image, the feature vector extracted from the histograms of texture feature maps is denoted as $h_i = \{h_{i,1}, h_{i,2}, \ldots, h_{i,70}\}$, while y_i and y_i' represent the ground

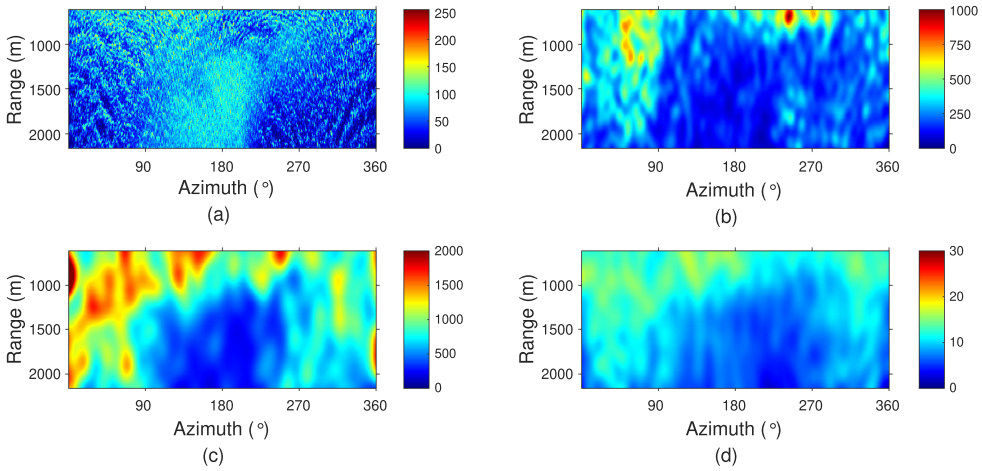

Fig. 6. (a) Rain-contaminated Decca radar image collected at 9:53, December 01. Anemometer-measured wind speed is 15.6 m/s. (b) Gabor texture feature map of (a) obtained from a Gabor filter with 5.7 in wavelength and 90° in orientation. (c) Gabor texture feature map of (a) obtained from a Gabor filter with 11.3 in wavelength and 90° in orientation. (d) DWT texture feature map of (a) obtained from the local standard deviation image of the low-low channel.

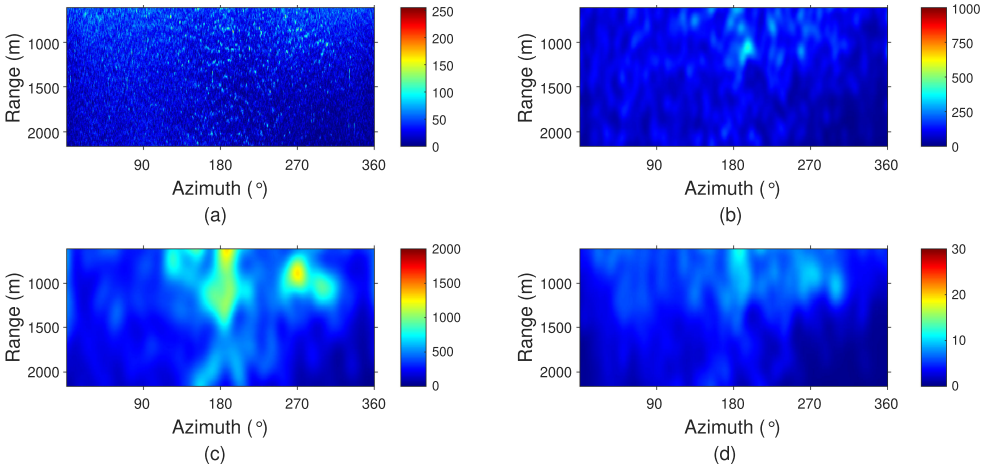

Fig. 7. (a) Rain-contaminated Decca radar image collected at 3:28, November 27. Anemometer-measured wind speed is 3.1 m/s. (b) Gabor texture feature map of (a) obtained from a Gabor filter with 5.7 in wavelength and 90° in orientation. (c) Gabor texture feature map of (a) obtained from a Gabor filter with 11.3 in wavelength and 90° in orientation. (d) DWT texture feature map of (a) obtained from the local standard deviation image of the low-low channel.

truth wind speed and radar-derived wind speed, respectively. As we know, in most linear regression models, the objective is to minimize the sum of squared errors. However, in many practical problems based on real data such as wind speed estimation, we are only concerned about reducing error to a certain degree as long as they fall within an acceptable range. SVR provides us with the flexibility to define how much error is acceptable in our model and find an appropriate hyperplane in higher dimensions to fit the data. Instead of minimizing the squared error in linear regression, the objective function of SVR is to minimize the coefficients, i.e., the l_2-norm of the coefficient vector (denoted as $||w||$). The error term is instead handled in the constraints, where we set the absolute error less than or equal to a specified margin, called the maximum error (denoted as ϵ). We can tune ϵ to gain the desired accuracy of our model. Therefore, the goal of training is to find a function $f(h_i)$ that has at most ϵ deviation from y_i while minimizing the norm of w at the same time [35]. Similar to [16], the classic ϵ-SVR algorithm proposed in [35] is employed to train the texture-feature-based wind speed estimation model. Thus, function can be expressed as

$$y_i' = f(h_i) = w^T \phi(h_i) + b \tag{12}$$

where $\phi(\cdot)$ is a Gaussian kernel function that maps h_i into a higher dimension space for linear separation, w is the weight of $\phi(h_i)$ and b is the bias term. According to the support vector machine (SVM) algorithm proposed in [36], finding such a function is equivalent to solving the following convex optimization problem

$$\min \left(\frac{1}{2} \|\boldsymbol{w}\|^2 + C \sum_{i=1}^{l} (\xi_i + \xi_i^*) \right) \tag{13}$$

subject to

$$\begin{cases} y_i - y_i' \leq \epsilon + \xi_i \\ y_i' - y_i \leq \epsilon + \xi_i^* \\ \xi_i, \xi_i^* \geq 0 \end{cases} \tag{14}$$

where ξ_i and ξ_i^* represent the values of estimation errors that are greater than ϵ, l is the total number of training samples. Since

TABLE I
TEXTURE FEATURE MAPS FOR HISTOGRAM FEATURE EXTRACTION

Texture Feature Type	Specification	Histogram Intensity Range	Num. of Bins
Gabor features	wavelength is 5.7, orientation is 90°	0 - 1000	20
Gabor features	wavelength is 11.3, orientation is 90°	0 - 2000	20
DWT features	the local standard deviation image of low-low channel	0 - 30	30

TABLE II
RADAR INFORMATION

	Decca	Koden
Installation site	Ship	Shore-based Tower
Polarization	Horizontal	Horizontal
Operating frequency	9.41 GHz	9.45 GHz
Pulse width	50 ns	80 ns
Range resolution	7.5 m	12 m
Range coverage	240 m - 2160 m	3 m - 6087 m
Beam width	2°	0.8°
Azimuth coverage	360°	190°
Antenna rotation speed	28 rpm	44 rpm
Antenna height	21.9 m	63 m
Backscatter intensity level	0 - 255	0 - 255

the existence of such errors is common when using real data for training, it is necessary to add the error terms into our objective function so that they can be minimized as much as possible. C is a positive constant named as box constraint, which determines the penalty imposed on y_i' that lies outside the ϵ margin and helps avoid overfitting. In this work, the regression learner toolbox from MATLAB is used to train the SVR-based wind estimation model, in which the sequential minimal optimization (SMO) algorithm proposed in [37] is adopted for solving the convex optimization problem.

III. EXPERIMENTAL RESULTS

A. Data Overview

Two radar image datasets collected from different sites are used to validate the effectiveness of the proposed method. A summary of the radar and dataset information is presented in Tables II and III. The first dataset, provided by Defence Research and Development Canada (DRDC), was collected during a sea trial in the North Atlantic Ocean off the East Coast of Canada. Specifically, the image data were obtained from a shipborne Decca radar, whose parameters are presented in Table II. By selecting the first pulse radar image generated per minute, a total of 3902 polar images were collected during several time periods from November 26 to December 4, 2008. Two sets of simultaneous wind information collected per minute by two anemometers mounted on the port and starboard of the ship, respectively, are averaged and used as ground truths. In addition, the presence of rain during data collection period can be indicated by the simultaneous rain rate information collected by two rain gauges installed on the ship.

The second dataset was provided by the Nearshore Remote Sensing Group of Oregon State University. A Koden marine radar was installed on a United States Coast Guard watchtower near the North Pacific Ocean, providing real-time radar images 24 h/d. A detailed description of the location information, radar and tower equipment can be found in [38]. In this study, 980 pulse images randomly collected from January 11 to July 18, 2019 with various time intervals are selected for wind parameter estimation. Since nearly half of the radar coverage area consists of land, the radar image only preserves azimuths that point toward the sea surface. The ground truth wind information was reported hourly by the weather station NWPO3 near the base of South Jetty of Yaquina Bay Inlet. It should be noted that the provided wind speed has already been averaged over a 2-min period, while wind direction was reported in 10° increments. In addition, rain rate data was obtained from rain station AS512 (ocrg.org) in the Newport residential area North of Yaquina Bay. It can be observed from Table III that both datasets cover a relatively wide range of wind speeds, rain rates, and wave heights (obtained from buoys deployed near radar sites), which permits the proposed method to be evaluated under various sea states and rain conditions.

TABLE III
DATASET INFORMATION

	Decca	Koden
Collection location	∼300 km south-southeast of Halifax, NS, Canada (42°30 N, 62°05 W)	USCG Station Yaquina Bay, Newport, OR, USA (44°62 N, 124°06 W)
Collection period	Nov. 26 - Dec. 4, 2008	Jan. 11 - Jul. 18, 2019
Wind speed range (m/s)	2.1 - 15.4	0 - 19.0
Ship speed range (m/s)	0 - 6.8	N/A
Significant wave height range (m)	1.5 - 5.0	0.6 - 7.2
Rain rate range (mm/h)	0 - 50.0	0 - 33.5
Number of images	3902	980

B. Rain Detection Results

In order to investigate the accuracy of the proposed scheme in rainy image detection, the global rainfall data provided by European Centre for Medium-Range Weather Forecasts (ECMWF) [39] are used as ground truth for comparison since they are derived from the advanced precipitation hindcasting techniques. Each value in the data corresponds to the accumulated rainfall in the previous hour (i.e., hourly average rain rate, mm/h) obtained from a certain measurement point. The distance between each adjacent measurement point (indicated by red dots in Fig. 8) in space is 0.25° in either latitude or longitude (around 27 km). Therefore, since the Decca radar was installed on a moving ship whose course is shown in Fig. 8, the hourly average rain rate is acquired from the measurement at the red dot that was closest to the ship location at that time. In Fig. 9, the hourly average rain rate values during the sea trial are depicted by the blue dotted line. It should be noted that radar data were not collected in several time periods during the sea trial and those periods are indicated by the black arrow lines between

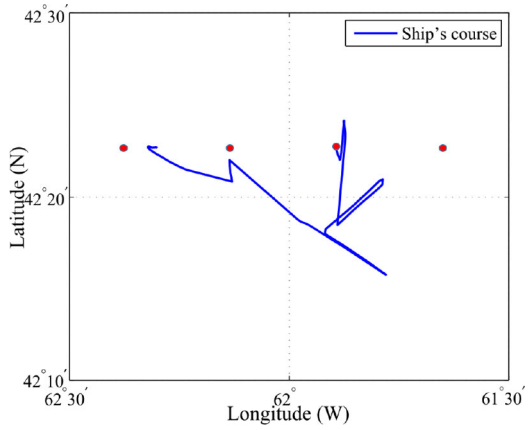

Fig. 8. Ship's course and available measurement points of rainfall.

the green dash lines. In order to show whether the proposed model can detect rainy images accurately using Decca radar data, the identification of rainy images using the proposed method is indicated by the gray shadows in Fig. 9. It can be observed that when hourly average rain rate is greater or equal to 1 mm/h, the presence of rainy images can always be detected (i.e., a detection success rate of 100%) among the 60 radar images obtained in each hour using the proposed model. On the other hand, when the hourly average rain rate is nonzero but less than 1 mm/h, rainy images might not be identified. That is because when the average rain rate is low, the presence of rainfall might be sparse in either time or space and is not within the radar coverage. Another possible reason is that under certain sea states (e.g., high wind speeds), the radar backscatter might not be altered significantly under low rain rates. As for the Koden radar data, they are not used to validate the rain detection accuracy because the time interval between each provided image is longer than an hour. Due to the fact that the rainfall distribution can be nonuniform in both time and space, as well as the fact that the radar coverage is much smaller than the spatial interval of each measurement point, it is likely that while rainfall was recorded, the only available radar image during this certain hour might not be affected by rain. Nevertheless, if more Koden radar images are available within a single hour, it is expected that the rainy images can be easily identified by thes model.

C. Wind Direction Results

The rain-correction result of Fig. 3(b) is presented in Fig. 3(c) and compared with Fig. 3(a), i.e., a rain-free radar image obtained from the same region under similar wind speeds. As shown in Fig. 3(e), the differences of normalized histogram bin values between two types of images are very small for most of the bins (no larger than 0.04), which indicates that both the rain-free and rain-corrected images have similar characteristics in pixel intensity distribution. Figs. 10 and 11 show the comparison of wind direction estimation results using the original rain-contaminated radar images without rain mitigation and rain-corrected images. As shown in Figs. 10(b) and 11(b), although it is impossible to fully recover the wave signatures contaminated by rain, the noise introduced by rain has been effectively suppressed. It can also be observed that the estimation errors can be reduced significantly for both the Decca (Fig. 10) and Koden data (Fig. 11) after introducing the proposed rain mitigation method.

Thus, in order to evaluate the effectiveness of the proposed method on rain mitigation quantitatively, for Decca radar data, all images are first input into the SOM-based identification model. In consequence, a total of 540 images that contain rain-contaminated regions are selected for wind estimation study. Fig. 12 shows the sequences of wind direction estimation results using rain-contaminated Decca radar images. As the time interval between each image in the same time period is one minute, both the anemometer and radar results are moving-averaged over 10 min. The root mean square deviation (RMSD) between wind directions derived using the proposed scheme (i.e, the red dots in Fig. 12) and measured by the anemometers (i.e., black line in Fig. 12) is 18.6°. In contrast, if the original rain-contaminated images are used directly for curve fitting without any correction, the RMSD is as high as 37.7°, as indicated by the blue dots in Fig. 12. Hence, the proposed method significantly improves the wind direction estimation accuracy with a reduction of 19.1° in RMSD.

As for the Koden radar data, the region presented in Fig. 11(a) is first cropped from the original radar image in order to avoid the influence of shore on sea clutter. As a result, the azimuth and range coverages of the region are around 135° and 5130 m, respectively. It should be noted that the images obtained under heavy precipitation or very low wind speeds ($\leq$2 m/s) with little or no wave signatures are excluded from wind direction estimation in order to ensure that all testing images contain sufficient electromagnetic backscatter from the ocean surface [40]. As the acquisition time interval between each image is relatively large, the wind direction estimation results obtained from 230 rain-contaminated images identified by the SOM-based model are presented as scatter plots in Fig. 13. Specifically, for Fig. 13(a), the curve fitting is applied to rain-contaminated radar images directly without correction, while Fig. 13(b) shows the results obtained from the rain-corrected images. Since the RMSDs between radar wind direction and anemometer wind direction calculated from Fig. 13(a) and (b) are 47.5° and 23.6°, respectively, the proposed scheme improves the estimation accuracy significantly, with a reduction of 23.9° in RMSD. Although the RMSD obtained from Koden images is 5.0° higher than using Decca images, it should be noted that the azimuth coverage in Koden images is only 135°, which indicates that it is more difficult to fit an accurate curve for wind direction estimation.

D. Wind Speed Results

For both datasets, nearly half of the rain-contaminated radar images are selected as training samples for the SVR-based wind speed estimation models. It should be noted that those samples should be obtained under a relatively wide range of wind speeds in order to ensure the models' robustness. The other half of the rain-contaminated images are all used to test

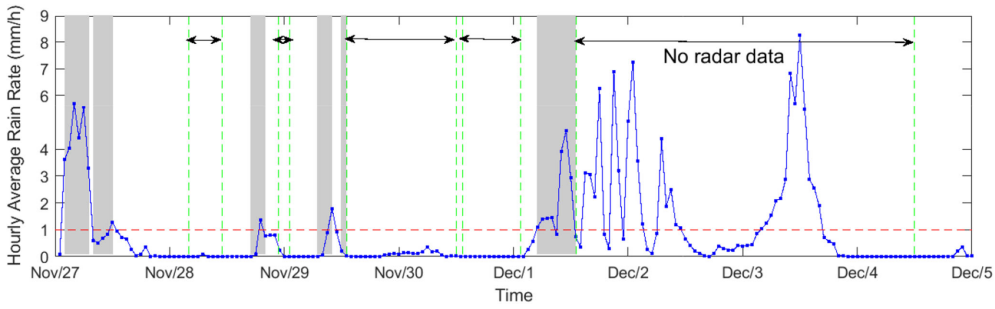

Fig. 9. Hourly average rain rate (dots connected by blue lines) values provided by ECMWF during Decca radar data collection periods. Simultaneous radar images with rainy regions detected by the proposed method are indicated by gray shadows.

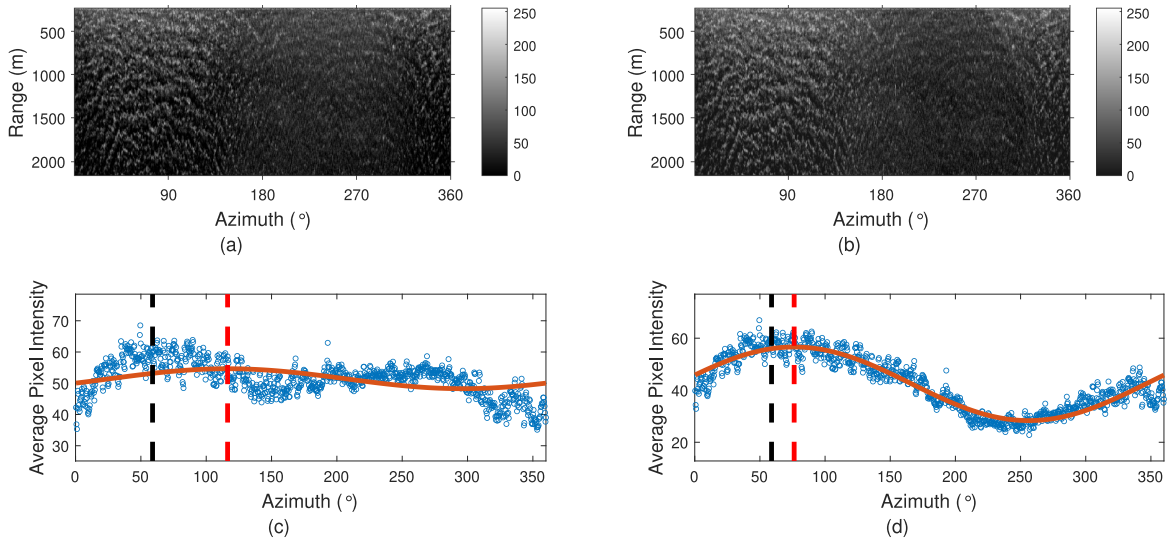

Fig. 10. (a) Example of a rain-contaminated Decca radar image. (b) Rain-corrected image obtained from (a) using the proposed method. (c) Wind direction estimation result using (a). (d) Wind direction estimation result using (b). The blue data points refer to the average pixel intensity in each azimuth of the radar image, while the orange line is the corresponding best-fit curve of the blue data points using the cosine-squared function. Red and black dash line indicate radar-derived wind direction and anemometer-measured wind direction, respectively.

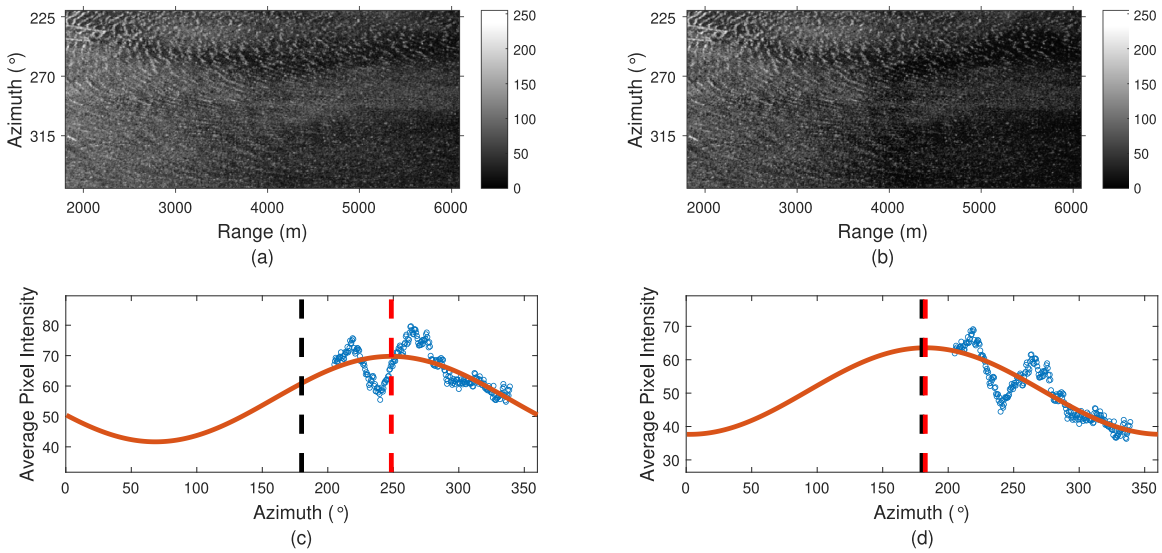

Fig. 11. (a) Example of a rain-contaminated Koden radar image. (b) Rain-corrected image obtained from (a) using the proposed method. (c) Wind direction estimation result using (a). (d) Wind direction estimation result using (b). The blue data points refer to the average pixel intensity in each azimuth of the radar image, while the orange line is the corresponding best-fit curve of the blue data points using the cosine-squared function. Red and black dash line indicate radar-derived wind direction and anemometer-measured wind direction, respectively.

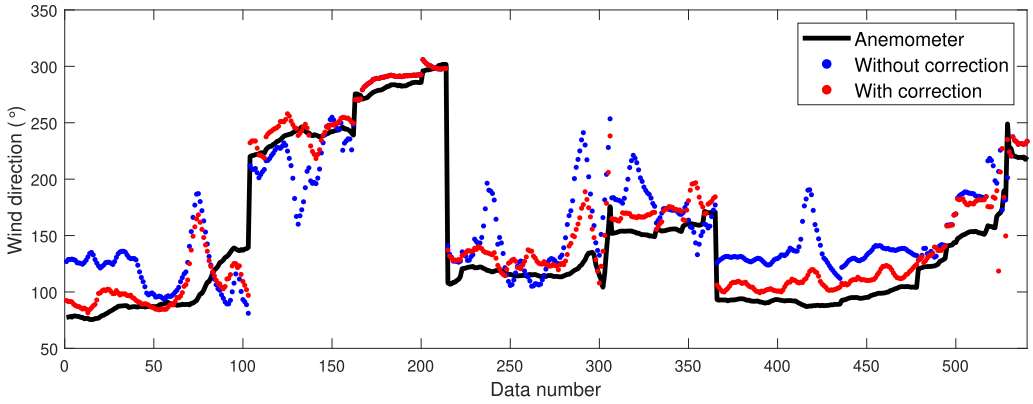

Fig. 12. Comparison of the sequences of Decca wind direction results.

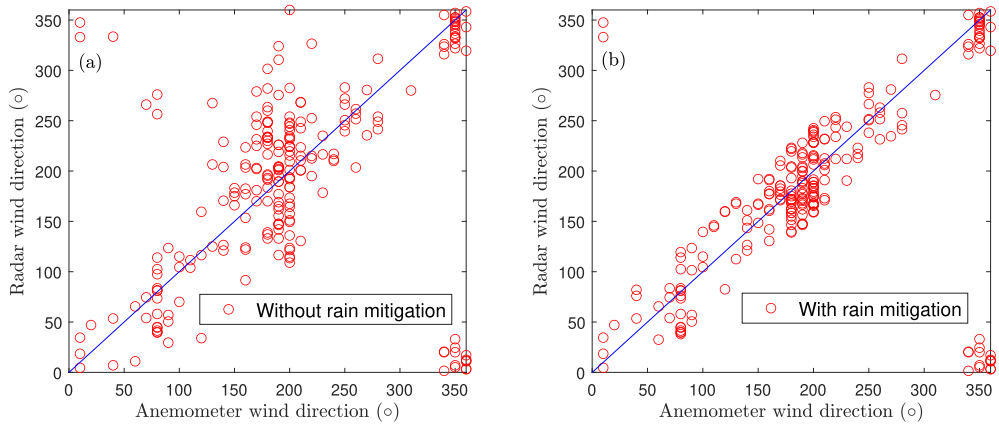

Fig. 13. Comparison of wind direction estimation results using (a) rain-contaminated Koden radar images without correction and (b) rain-corrected Koden radar images.

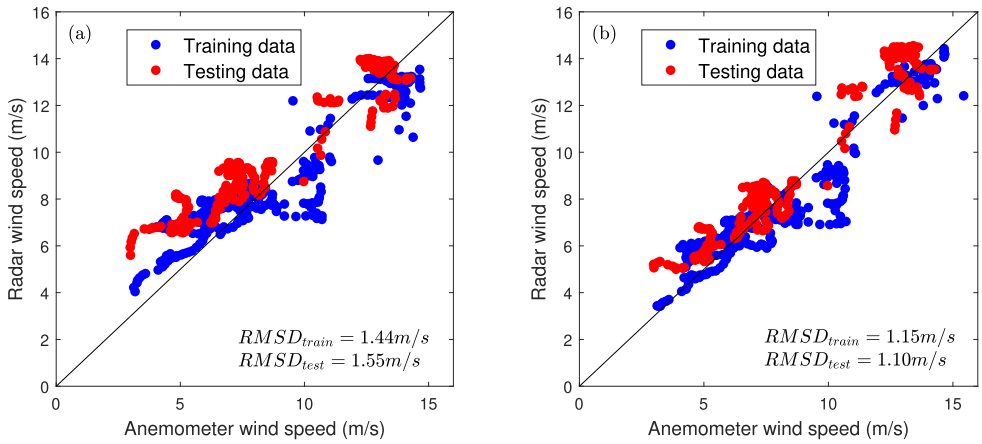

Fig. 14. Comparison of wind speed estimation results using (a) rain-contaminated Decca radar images without correction and (b) rain-corrected Decca radar images.

the models' accuracy. In addition, in order to validate the effectiveness of the proposed rain mitigation method, for each dataset two models are trained and tested separately using the original and rain-corrected radar images, respectively. The wind speed estimation results obtained from the Decca radar data are shown in Fig. 14 with both the anemometer and radar results being moving-averaged over 10 min. By comparing the results presented in Fig. 14(a) and (b), it can be observed that the proposed rain correction method further improves estimation accuracy in both training and testing samples. In particular, the RMSD between testing images and anemometer measurements is reduced by 0.45 m/s.

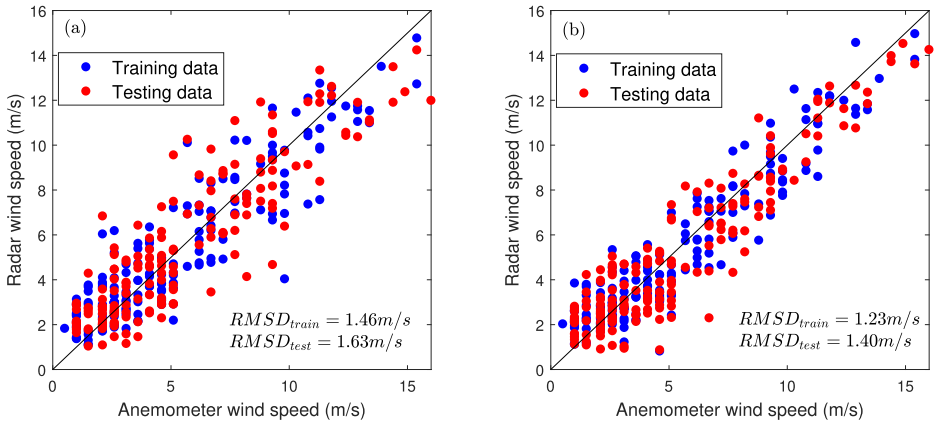

Fig. 15. Comparison of wind speed estimation results using (a) rain-contaminated Koden radar images without correction and (b) rain-corrected Koden radar images.

TABLE IV
WIND ESTIMATION STATISTICS RESULTS

Dataset	Wind direction				Wind speed							
	Without correction		With correction		Without correction				With correction			
					Training		Testing		Training		Testing	
	RMSD (○)	CC	RMSD (○)	CC	RMSD (○)	CC	RMSD (○)	CC	RMSD (○)	CC	RMSD (○)	CC
Decca	36.7	0.89	18.6	0.98	1.44	0.88	1.55	0.93	1.15	0.90	1.10	0.94
Koden	47.5	0.88	23.6	0.96	1.46	0.91	1.63	0.90	1.23	0.94	1.40	0.93

As for the Koden radar data, since the texture features extracted from each image are no longer dependent on the azimuthal intensity information, images obtained under low wind speeds (except zero wind speed) may still be utilized for wind speed estimation. Thus, a total of 350 rain-contaminated images identified by the SOM-based model are used to train and test the proposed wind speed estimation model. The estimation results obtained from models using original radar data (i.e., rain-contaminated images without correction) and rain-corrected images are presented in Fig. 15(a) and (b), respectively. Hence, it can be concluded that the proposed rain mitigation method improves both training and testing accuracy, with a reduction of 0.23 m/s in RMSD for both samples. Nevertheless, it should be noted that the RMSD obtained from the Koden radar data is generally higher than that of the Decca radar data. One reason may be due to the fact that compared to the Decca radar data, a relatively large portion of rain-contaminated Koden images were obtained under low wind speeds ($\leq$4 m/s) with little wave signatures. In consequence, texture features extracted from those images are more likely to be similar to each other, which makes it hard to provide highly precise estimation. Thus, it can be concluded that although the texture-feature-incorporated SVR-based wind speed estimation method is already more accurate than previous proposed models, introducing rain correction procedure will further improve measurement accuracy. To sum up, the RMSDs and correlation coefficients (CCs) of the wind speed and direction results for different schemes and radar datasets are shown in Table IV. It can be clearly observed that all the CC values are improved after introducing the proposed rain correction techniques. In the end, in order to ensure the proposed scheme can be implemented in real-time, the testing was conducted in MATLAB R2019b installed on a normal PC running Windows 10 with a 3.0 GHz Intel Core i5-2320 CPU, 8 GB memory, and a 64-bit operating system. For each rain-contaminated radar image it took an average of around 45 s to conduct rain correction and generate wind estimation results.

IV. CONCLUSION

In this study, a novel scheme to mitigate the rain influence and estimate sea surface wind parameters from rain-contaminated marine radar images is proposed. In order to detect the presence of rain, texture features extracted from radar data are input into an SOM-based model, which generates pixel-based rain identification results. Then, an image dehazing CNN called DehazeNet is applied to images that contain rain-contaminated pixels, which produces a transmission map reflecting the degree of rain influence. The influence of rain can therefore be corrected by inputting both the transmission map and the original image into the atmospheric scattering model. After obtaining rain-corrected radar images, wind direction can be estimated by curve fitting on average azimuthal intensities. As for wind speed, normalized histogram bin values extracted from three texture feature maps are combined as feature vectors to train the SVR-based wind speed estimation models.

Both shipborne (Decca) and shore-based radar (Koden) datasets are employed to validate the proposed scheme, with simultaneous anemometer measurements used as ground truths to evaluate estimation accuracy. In addition, in order to validate the effectiveness of the proposed rain correction method, wind measurements using original rain-contaminated images without correction are also conducted for comparison. For wind direction

estimation, the RMSDs obtained using the proposed scheme are 18.6° for the Decca radar images and 23.6° for the Koden radar images, respectively. Compared to the results obtained without applying rain correction, the estimation errors are reduced significantly, with RMSDs decreased by 19.1° and 23.9° for the Decca and Koden data, respectively. While for wind speed estimation, for both datasets, two SVR-based models are trained and tested separately under a wide range of wind speeds, with one using rain-contaminated images without correction and another using rain-corrected images, respectively. Results show that compared to the SVR-based models trained using the original radar images, the rain-corrected SVR-based models further improve both training and testing accuracy. Specifically, the RMSDs calculated from rain-corrected testing samples are 1.10 and 1.40 m/s for the Decca and Koden data, respectively, which are 0.45 and 0.23 m/s lower than that obtained from the original rain-contaminated images. Since rain echoes are more likely to overwhelm wave signatures under low wind speeds, the proposed method produces better results at higher wind speeds than lower wind speeds. In addition, as it takes around 45 s to obtain rain correction and wind estimation results from each rain-contaminated radar image, the proposed scheme can be implemented in real time.

As the first work to apply pixel-based rain identification model and image dehazing techniques for wind parameter measurements using X-band marine radar images, the proposed method effectively improves the accuracy of wind estimation from rain-contaminated data. Also, this is the first method validated using rain-contaminated shore-based marine radar images with limited azimuthal coverage. Despite the significant reduction of estimation errors achieved by the proposed method, it should be noted that the wind direction estimation results are still not as accurate as that obtained from previous studies using rain-free radar data. As the SVR-based wind speed estimation models have received satisfactory results, it is worthwhile to develop machine learning-based algorithms for wind direction estimation. Due to similar imaging mechanisms, it is also possible to extend the proposed method to radar images captured at other frequency bands such as S-band, which is another common frequency band for commercial marine radars. Although compared to the X-band radar, the S-band radar gives a coarser spatial resolution, previous studies have found that the influence of rain on S-band radar images is less severe than that on X-band radar images [41]. In addition, the effectiveness of the proposed rain correction scheme should be further validated on the estimation of other parameters (e.g., surface wave and current parameters) in future work.

ACKNOWLEDGMENT

The authors would like to thank Dr. E. Thornhill of Defence Research and Development Canada, as well as R. Pittman from the Nearshore Remote Sensing Group at Oregon State University for providing the radar, anemometer, buoy, and rain gauge data. OSU radar station is supported by NANOOS (NOAA).

REFERENCES

[1] W. Huang, X. Liu, and E. Gill, "Ocean wind and wave measurements using X-band marine radar: A comprehensive review," *Remote Sens.*, vol. 9, no. 12, Jan. 2017, Art. no. 1261.

[2] B. Lund, H. C. Graber, and R. Romeiser, "Wind retrieval from shipborne nautical X-band radar data," *IEEE Trans. Geosci. Remote Sens.*, vol. 50, no. 10, pp. 3800–3811, Oct. 2012.

[3] P. Lee *et al.*, "Wind-speed dependence of small-grazing-angle microwave backscatter from sea surfaces," *IEEE Trans. Antennas Propag.*, vol. 44, no. 3, pp. 333–340, Mar. 1996.

[4] D. B. Trizna and D. J. Carlson, "Studies of dual polarized low grazing angle radar sea scatter in nearshore regions," *IEEE Trans. Geosci. Remote Sens.*, vol. 34, no. 3, pp. 747–757, May 1996.

[5] H. Dankert, J. Horstmann, and W. Rosenthal, "Wind-and wave-field measurements using marine X-band radar-image sequences," *IEEE J. Ocean. Eng.*, vol. 30, no. 3, pp. 534–542, Jul. 2005.

[6] H. Dankert and J. Horstmann, "A marine radar wind sensor," *J. Atmospheric Ocean. Technol.*, vol. 24, no. 9, pp. 1629–1631, 1633–1642, Sep. 2007.

[7] R. Vicen-Bueno, J. Horstmann, E. Terril, T. de Paolo, and J. Dannenberg, "Real-time ocean wind vector retrieval from marine radar image sequences acquired at grazing angle," *J. Atmospheric Ocean. Technol.*, vol. 30, no. 1, pp. 127–139, 2013.

[8] Z. Chen, Y. He, B. Zhang, and Z. Qiu, "Determination of nearshore sea surface wind vector from marine X-band radar images," *Ocean Eng.*, vol. 96, pp. 79–85, 2015.

[9] Y. Liu, W. Huang, E. W. Gill, D. K. Peters, and R. Vicen-Bueno, "Comparison of algorithms for wind parameters extraction from shipborne X-band marine radar images," *IEEE J. Sel. Topics Appl. Earth Observ. Remote Sens.*, vol. 8, no. 2, pp. 896–906, Feb. 2015.

[10] X. Chen, W. Huang, C. Zhao, and Y. Tian, "Rain detection from X-band marine radar images: A support vector machine-based approach," *IEEE Trans. Geosci. Remote Sens.*, vol. 58, no. 3, pp. 2115–2123, Mar. 2020.

[11] W. Huang and E. W. Gill, "Ocean remote sensing using X-band shipborne nautical radar-applications in eastern Canada," in *Coastal Ocean Observing Syst.*, 2015, pp. 248–264.

[12] Y. Wang and W. Huang, "An algorithm for wind direction retrieval from X-band marine radar images," *IEEE Geosci. Remote Sens. Lett.*, vol. 13, no. 2, pp. 252–256, Feb. 2016.

[13] W. Huang and Y. Wang, "A spectra-analysis-based algorithm for wind speed estimation from X-band nautical radar images," *IEEE Geosci. Remote Sens. Lett.*, vol. 13, no. 5, pp. 701–705, May 2016.

[14] W. Huang, Y. Liu, and E. W. Gill, "Texture-analysis-incorporated wind parameters extraction from rain-contaminated X-band nautical radar images," *Remote Sens.*, vol. 9, no. 2, 2017, Art. no. 166.

[15] W. Huang, X. Liu, and E. W. Gill, "An empirical mode decomposition method for sea surface wind measurements from X-band nautical radar data," *IEEE Trans. Geosci. Remote Sens.*, vol. 55, no. 11, pp. 6218–6227, Nov. 2017.

[16] X. Chen, W. Huang, and G. Yao, "Wind speed estimation from X-band marine radar images using support vector regression method," *IEEE Geosci. Remote Sens. Lett.*, vol. 15, no. 9, pp. 1312–1316, Sep. 2018.

[17] X. Chen and W. Huang, "Identification of rain and low-backscatter regions in X-band marine radar images: An unsupervised approach," *IEEE Trans. Geosci. Remote Sens.*, vol. 58, no. 6, pp. 4225–4236, Jun. 2020.

[18] B. Cai, X. Xu, K. Jia, C. Qing, and D. Tao, "Dehazenet: An end-to-end system for single image haze removal," *IEEE Trans. Image Process.*, vol. 25, no. 11, pp. 5187–5198, Nov. 2016.

[19] L. Cornejo-Bueno, J. N. Borge, E. Alexandre, K. Hessner, and S. Salcedo-Sanz, "Accurate estimation of significant wave height with support vector regression algorithms and marine radar images," *Coastal Eng.*, vol. 114, pp. 233–243, 2016.

[20] X. Chen and W. Huang, "Gaussian process regression for estimating wind speed from X-band marine radar images," in *Proc. OEANS MTS/IEEE Charleston*, USA, 2018, pp. 1–4.

[21] X. Chen and W. Huang, "Automatic identification of rain-contaminated regions in X-band marine radar images," in *Proc. MTS/IEEE Oceans*, Seattle, USA, 2019, pp. 1–4.

[22] J. An, W. Huang, and E. W. Gill, "A self-adaptive wavelet-based algorithm for wave measurement using nautical radar," *IEEE Trans. Geosci. Remote Sens.*, vol. 53, no. 1, pp. 567–577, Jan. 2015.

[23] P. Chernyshov, T. Vrecica, M. Streßer, R. Carrasco, and Y. Toledo, "Rapid wavelet-based bathymetry inversion method for nearshore X-band radars," *Remote Sens. Environ.*, vol. 240, 2020, Art. no. 111688.

[24] I. Ng, T. Tan, and J. Kittler, "On local linear transform and Gabor filter representation of texture," in *Proc., Int. Conf. Pattern Recognit.*, 1992, pp. 627–631.
[25] R. T. Tan, "Visibility in bad weather from a single image," in *Proc. IEEE Conf. Comput. Vision Pattern Recognit.*, Jun. 2008, pp. 1–8.
[26] K. He, J. Sun, and X. Tang, "Single image haze removal using dark channel prior," *IEEE Trans. Pattern Anal. Mach. Intell.*, vol. 33, no. 12, pp. 2341–2353, Dec. 2011.
[27] Q. Zhu, J. Mai, and L. Shao, "A fast single image haze removal algorithm using color attenuation prior," *IEEE Trans. Image Process.*, vol. 24, no. 11, pp. 3522–3533, Nov. 2015.
[28] X. Liu, W. Huang, and E. W. Gill, "Analysis of rain effects on wave height estimation from X-band nautical radar images," in *Proc. MTS/IEEE Oceans*, Washington, USA, 2015, pp. 1–4.
[29] K. Tang, J. Yang, and J. Wang, "Investigating haze-relevant features in a learning framework for image dehazing," in *Proc. IEEE Conf. Comput. Vision Pattern Recognit.*, Jun. 2014, pp. 2995–3000.
[30] K. He, J. Sun, and X. Tang, "Guided image filtering," *IEEE Trans. Pattern Anal. Mach. Intell.*, vol. 35, no. 6, pp. 1397–1409, Jun. 2013.
[31] S. G. Narasimhan and S. K. Nayar, "Vision and the atmosphere," *Int. J. Comput. Vis.*, vol. 48, no. 3, pp. 233–254, 2002.
[32] R. Fattal, "Single image dehazing," *ACM Trans. Graph.*, vol. 27, no. 3, 2008, Art. no. 72.
[33] O. Phillips, "On the dynamics of unsteady gravity waves of finite amplitude Part 1. The elementary interactions," *J. Fluid Mechanics*, vol. 9, no. 2, pp. 193–217, 1960.
[34] Z. Chen, Y. He, B. Zhang, and Y. Ma, "A method to correct the influence of rain on X-band marine radar image," *IEEE Access*, vol. 5, pp. 25576–25583, 2017.
[35] A. J. Smola and B. Schölkopf, "A tutorial on support vector regression," *Statist. Comput.*, vol. 14, no. 3, pp. 199–222, 2004.
[36] C. Cortes and V. Vapnik, "Support-vector networks," *Mach. Learn.*, vol. 20, no. 3, pp. 273–297, 1995.
[37] R.-E. Fan, P.-H. Chen, and C.-J. Lin, "Working set selection using second order information for training support vector machines," *J. Mach. Learn. Res.*, vol. 6, pp. 1889–1918, 2005.
[38] M. C. Haller, D. A. Honegger, R. Pittman, A. O'Dea, and A. Simpson, "Real-time marine radar observations of nearshore waves and flow structures from shore-based towers," in *Proc. IEEE/OES 12th Current, Waves Turbulence Meas.*, San Diego, USA, 2019, pp. 1–7.
[39] *Copernicus Climate Data Store*. Accessed: Dec. 18, 2020. [Online]. Available: https://cds.climate.copernicus.eu/cdsapp#!/home
[40] R. Gangeskar, "Verifying high-accuracy ocean surface current measurements by X-band radar for fixed and moving installations," *IEEE Trans. Geosci. Remote Sens.*, vol. 56, no. 8, pp. 4845–4855, Aug. 2018.
[41] H.-Y. Cheng and H. Chien, "Implementation of S-band marine radar for surface wave measurement under precipitation," *Remote Sens. Environ.*, vol. 188, pp. 85–94, 2017.

Xinwei Chen (Student Member, IEEE) was born in Guangzhou, China. He received the B.Eng. degree in information engineering from the South China University of Technology, Guangzhou, China, in 2017. He is currently working toward the Ph.D. degree in electrical engineering with the Memorial University of Newfoundland, St. John's, NL, Canada.

His research interests include X-band marine radar ocean surface remote sensing.

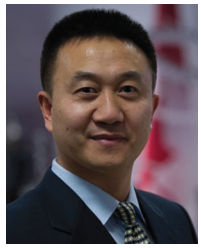

Weimin Huang (Senior Member, IEEE) received the B.S., M.S., and Ph.D. degrees in radio physics from Wuhan University, Wuhan, China, in 1995, 1997, and 2001, respectively, and the M.Eng. degree in electrical engineering from the Memorial University of Newfoundland, St. John's, NL, Canada, in 2004.

From 2008 to 2010, he was a Design Engineer with Rutter Technologies, St. John's, NL, Canada. Since 2010, he has been with the Faculty of Engineering and Applied Science, Memorial University of Newfoundland, St. John's, NL, USA, where he is currently a Professor. He has authored more than 250 research papers. His research interests include the mapping of oceanic surface parameters via high-frequency ground wave radar, X-band marine radar, and global navigation satellite systems.

Dr. Huang was the recipient of the Postdoctoral Fellowship from Memorial University of Newfoundland. He was the recipient of the Discovery Accelerator Supplements Award from the Natural Sciences and Engineering Research Council of Canada, in 2017, and the recipient of the IEEE Geoscience and Remote Sensing Society 2019 Letters Prize Paper Award. He is currently an Area Editor for the IEEE CANADIAN JOURNAL OF ELECTRICAL AND COMPUTER ENGINEERING, an Associate Editor for IEEE ACCESS, an Editorial Board Member for *Remote Sensing*, and a Guest Editor for IEEE JOURNAL OF SELECTED TOPICS IN APPLIED EARTH OBSERVATIONS AND REMOTE SENSING. He serves as a regular Reviewer over 60 international journals and a Reviewer for many IEEE international conferences, such as RadarCon, International Conference on Communications, IEEE Global Communications Conference, IEEE Geoscience and Remote Sensing Society, and Oceans. He has been a Technical Program Committee Member. He served as a Technical Program Co-Chair of the IEEE Newfoundland Electrical and Computer Engineering Conference, in 2012 and 2013.

Merrick C. Haller (Senior Member, IEEE) received the Ph.D. degree in civil engineering from the University of Delaware, Newark, DE, USA, in 1999.

He spent two years in the remote sensing industry before joining Oregon State University, Corvallis, OR, USA, in 2001, where he is currently a Professor and an Associate School Head with the School of Civil and Construction Engineering. His research interests include development of remote sensing techniques for the study of coastal ocean processes including: Wave breaking, rip currents, internal wave propagation, and submesoscale fronts.